Y cross section in p + p collisions at √s = 200 GeV

(STAR Collaboration) Abelev, B. I.; ...; Planinić, Mirko; ...; Poljak, Nikola; ...; Zoulkarneeva, Y.

Υ cross section in $p + p$ collisions at $\sqrt{s} = 200$ GeV

B. I. Abelev,[8] M. M. Aggarwal,[30] Z. Ahammed,[47] A. V. Alakhverdyants,[17] B. D. Anderson,[18] D. Arkhipkin,[3]
G. S. Averichev,[17] J. Balewski,[22] L. S. Barnby,[2] S. Baumgart,[52] D. R. Beavis,[3] R. Bellwied,[50] M. J. Betancourt,[22]
R. R. Betts,[8] A. Bhasin,[16] A. K. Bhati,[30] H. Bichsel,[49] J. Bielcik,[10] J. Bielcikova,[11] B. Biritz,[6] L. C. Bland,[3] B. E. Bonner,[36]
J. Bouchet,[18] E. Braidot,[27] A. V. Brandin,[25] A. Bridgeman,[1] E. Bruna,[52] S. Bueltmann,[29] I. Bunzarov,[17] T. P. Burton,[2]
X. Z. Cai,[40] H. Caines,[52] M. Calderón de la Barca Sánchez,[5] O. Catu,[52] D. Cebra,[5] R. Cendejas,[6] M. C. Cervantes,[42]
Z. Chajecki,[28] P. Chaloupka,[11] S. Chattopadhyay,[47] H. F. Chen,[38] J. H. Chen,[40] J. Y. Chen,[51] J. Cheng,[44] M. Cherney,[9]
A. Chikanian,[52] K. E. Choi,[34] W. Christie,[3] P. Chung,[11] R. F. Clarke,[42] M. J. M. Codrington,[42] R. Corliss,[22]
M. R. Cosentino,[37] J. G. Cramer,[49] H. J. Crawford,[4] D. Das,[5] S. Dash,[13] A. Davila Leyva,[43] L. C. De Silva,[50] R. R. Debbe,[3]
T. G. Dedovich,[17] M. DePhillips,[3] A. A. Derevschikov,[32] R. Derradi de Souza,[7] L. Didenko,[3] P. Djawotho,[42] S. M. Dogra,[16]
X. Dong,[21] J. L. Drachenberg,[42] J. E. Draper,[5] J. C. Dunlop,[3] M. R. Dutta Mazumdar,[47] L. G. Efimov,[17] E. Elhalhuli,[2]
M. Elnimr,[50] J. Engelage,[4] G. Eppley,[36] B. Erazmus,[41] M. Estienne,[41] L. Eun,[31] O. Evdokimov,[8] P. Fachini,[3] R. Fatemi,[19]
J. Fedorisin,[17] R. G. Fersch,[19] P. Filip,[17] E. Finch,[52] V. Fine,[3] Y. Fisyak,[3] C. A. Gagliardi,[42] D. R. Gangadharan,[6]
M. S. Ganti,[47] E. J. Garcia-Solis,[8] A. Geromitsos,[41] F. Geurts,[36] V. Ghazikhanian,[6] P. Ghosh,[47] Y. N. Gorbunov,[9]
A. Gordon,[3] O. Grebenyuk,[21] D. Grosnick,[46] B. Grube,[34] S. M. Guertin,[6] A. Gupta,[16] N. Gupta,[16] W. Guryn,[3] B. Haag,[5]
T. J. Hallman,[3] A. Hamed,[42] L-X. Han,[40] J. W. Harris,[52] J. P. Hays-Wehle,[22] M. Heinz,[52] S. Heppelmann,[31] A. Hirsch,[33]
E. Hjort,[21] A. M. Hoffman,[22] G. W. Hoffmann,[43] D. J. Hofman,[8] R. S. Hollis,[8] H. Z. Huang,[6] T. J. Humanic,[28] L. Huo,[42]
G. Igo,[6] A. Iordanova,[8] P. Jacobs,[21] W. W. Jacobs,[15] P. Jakl,[11] C. Jena,[13] F. Jin,[40] C. L. Jones,[22] P. G. Jones,[2] J. Joseph,[18]
E. G. Judd,[4] S. Kabana,[41] K. Kajimoto,[43] K. Kang,[44] J. Kapitan,[11] K. Kauder,[8] D. Keane,[18] A. Kechechyan,[17] D. Kettler,[49]
D. P. Kikola,[21] J. Kiryluk,[21] A. Kisiel,[48] A. G. Knospe,[52] A. Kocoloski,[22] D. D. Koetke,[46] T. Kollegger,[12] J. Konzer,[33]
M. Kopytine,[18] I. Koralt,[29] W. Korsch,[19] L. Kotchenda,[25] V. Kouchpil,[11] P. Kravtsov,[25] K. Krueger,[1] M. Krus,[10]
L. Kumar,[30] P. Kurnadi,[6] M. A. C. Lamont,[3] J. M. Landgraf,[3] S. LaPointe,[50] J. Lauret,[3] A. Lebedev,[3] R. Lednicky,[17]
C-H. Lee,[34] J. H. Lee,[3] W. Leight,[22] M. J. LeVine,[3] C. Li,[38] L. Li,[43] N. Li,[51] W. Li,[40] X. Li,[33] X. Li,[39] Y. Li,[44] Z. Li,[51]
G. Lin,[52] S. J. Lindenbaum,[26,*] M. A. Lisa,[28] F. Liu,[51] H. Liu,[5] J. Liu,[36] T. Ljubicic,[3] W. J. Llope,[36] R. S. Longacre,[3]
W. A. Love,[3] Y. Lu,[38] G. L. Ma,[40] Y. G. Ma,[40] D. P. Mahapatra,[13] R. Majka,[52] O. I. Mall,[5] L. K. Mangotra,[16]
R. Manweiler,[46] S. Margetis,[18] C. Markert,[43] H. Masui,[21] H. S. Matis,[21] Yu. A. Matulenko,[32] D. McDonald,[36]
T. S. McShane,[9] A. Meschanin,[32] R. Milner,[22] N. G. Minaev,[32] S. Mioduszewski,[42] A. Mischke,[27] M. K. Mitrovski,[12]
B. Mohanty,[47] M. M. Mondal,[47] D. A. Morozov,[32] M. G. Munhoz,[37] B. K. Nandi,[14] C. Nattrass,[52] T. K. Nayak,[47]
J. M. Nelson,[2] P. K. Netrakanti,[33] M. J. Ng,[4] L. V. Nogach,[32] S. B. Nurushev,[32] G. Odyniec,[21] A. Ogawa,[3] H. Okada,[3]
V. Okorokov,[25] D. Olson,[21] M. Pachr,[10] B. S. Page,[15] S. K. Pal,[47] Y. Pandit,[18] Y. Panebratsev,[17] T. Pawlak,[48]
T. Peitzmann,[27] V. Perevoztchikov,[3] C. Perkins,[4] W. Peryt,[48] S. C. Phatak,[13] P. Pile,[3] M. Planinic,[53] M. A. Ploskon,[21]
J. Pluta,[48] D. Plyku,[29] N. Poljak,[53] A. M. Poskanzer,[21] B. V. K. S. Potukuchi,[16] C. B. Powell,[21] D. Prindle,[49] C. Pruneau,[50]
N. K. Pruthi,[30] P. R. Pujahari,[14] J. Putschke,[52] R. Raniwala,[35] S. Raniwala,[35] R. L. Ray,[43] R. Redwine,[22] R. Reed,[5]
J. M. Rehberg,[12] H. G. Ritter,[21] J. B. Roberts,[36] O. V. Rogachevskiy,[17] J. L. Romero,[5] A. Rose,[21] C. Roy,[41] L. Ruan,[3]
R. Sahoo,[41] S. Sakai,[6] I. Sakrejda,[21] T. Sakuma,[22] S. Salur,[5] J. Sandweiss,[52] J. Schambach,[43]
R. P. Scharenberg,[33] N. Schmitz,[23] T. R. Schuster,[12] J. Seele,[22] J. Seger,[9] I. Selyuzhenkov,[15] P. Seyboth,[23] E. Shahaliev,[17]
M. Shao,[38] M. Sharma,[50] S. S. Shi,[51] E. P. Sichtermann,[21] F. Simon,[23] R. N. Singaraju,[47] M. J. Skoby,[33] N. Smirnov,[52]
P. Sorensen,[3] J. Sowinski,[15] H. M. Spinka,[1] B. Srivastava,[33] T. D. S. Stanislaus,[46] D. Staszak,[6] J. R. Stevens,[15] R. Stock,[12]
M. Strikhanov,[25] B. Stringfellow,[33] A. A. P. Suaide,[37] M. C. Suarez,[8] N. L. Subba,[18] M. Sumbera,[11] X. M. Sun,[21] Y. Sun,[38]
Z. Sun,[20] B. Surrow,[22] T. J. M. Symons,[21] A. Szanto de Toledo,[37] J. Takahashi,[7] A. H. Tang,[3] Z. Tang,[38] L. H. Tarini,[50]
T. Tarnowsky,[24] D. Thein,[43] J. H. Thomas,[21] J. Tian,[40] A. R. Timmins,[50] S. Timoshenko,[25] D. Tlusty,[11] M. Tokarev,[17]
T. A. Trainor,[49] V. N. Tram,[21] S. Trentalange,[6] R. E. Tribble,[42] O. D. Tsai,[6] J. Ulery,[33] T. Ullrich,[3] D. G. Underwood,[1]
G. Van Buren,[3] M. van Leeuwen,[27] G. van Nieuwenhuizen,[22] J. A. Vanfossen, Jr.,[18] R. Varma,[14] G. M. S. Vasconcelos,[7]
A. N. Vasiliev,[32] F. Videbaek,[3] Y. P. Viyogi,[47] S. Vokal,[17] S. A. Voloshin,[50] M. Wada,[43] M. Walker,[22] F. Wang,[33] G. Wang,[6]
H. Wang,[24] J. S. Wang,[20] Q. Wang,[33] X. L. Wang,[38] Y. Wang,[44] G. Webb,[19] J. C. Webb,[3] G. D. Westfall,[24] C. Whitten, Jr.,[6]
H. Wieman,[21] E. Wingfield,[43] S. W. Wissink,[15] R. Witt,[45] Y. Wu,[51] W. Xie,[33] N. Xu,[21] Q. H. Xu,[39] W. Xu,[6] Y. Xu,[38] Z. Xu,[3]
L. Xue,[40] Y. Yang,[20] P. Yepes,[36] K. Yip,[3] I-K. Yoo,[34] Q. Yue,[44] M. Zawisza,[48] H. Zbroszczyk,[48] W. Zhan,[20] S. Zhang,[40]
W. M. Zhang,[18] X. P. Zhang,[21] Y. Zhang,[21] Z. P. Zhang,[38] J. Zhao,[40] C. Zhong,[40] J. Zhou,[36] W. Zhou,[39] X. Zhu,[44]
Y. H. Zhu,[40] R. Zoulkarneev,[17] and Y. Zoulkarneeva[17]

(STAR Collaboration)

[1]*Argonne National Laboratory, Argonne, Illinois 60439, USA*
[2]*University of Birmingham, Birmingham, United Kingdom*
[3]*Brookhaven National Laboratory, Upton, New York 11973, USA*
[4]*University of California, Berkeley, California 94720, USA*
[5]*University of California, Davis, California 95616, USA*
[6]*University of California, Los Angeles, California 90095, USA*
[7]*Universidade Estadual de Campinas, Sao Paulo, Brazil*
[8]*University of Illinois at Chicago, Chicago, Illinois 60607, USA*
[9]*Creighton University, Omaha, Nebraska 68178, USA*
[10]*Czech Technical University in Prague, FNSPE, Prague, 115 19, Czech Republic*
[11]*Nuclear Physics Institute AS CR, 250 68 Řež/Prague, Czech Republic*
[12]*University of Frankfurt, Frankfurt, Germany*
[13]*Institute of Physics, Bhubaneswar 751005, India*
[14]*Indian Institute of Technology, Mumbai, India*
[15]*Indiana University, Bloomington, Indiana 47408, USA*
[16]*University of Jammu, Jammu 180001, India*
[17]*Joint Institute for Nuclear Research, Dubna, 141 980, Russia*
[18]*Kent State University, Kent, Ohio 44242, USA*
[19]*University of Kentucky, Lexington, Kentucky 40506-0055, USA*
[20]*Institute of Modern Physics, Lanzhou, China*
[21]*Lawrence Berkeley National Laboratory, Berkeley, California 94720, USA*
[22]*Massachusetts Institute of Technology, Cambridge, Massachusetts 02139-4307, USA*
[23]*Max-Planck-Institut für Physik, Munich, Germany*
[24]*Michigan State University, East Lansing, Michigan 48824, USA*
[25]*Moscow Engineering Physics Institute, Moscow, Russia*
[26]*City College of New York, New York City, New York 10031, USA*
[27]*NIKHEF and Utrecht University, Amsterdam, The Netherlands*
[28]*The Ohio State University, Columbus, Ohio 43210, USA*
[29]*Old Dominion University, Norfolk, Virginia, 23529, USA*
[30]*Panjab University, Chandigarh 160014, India*
[31]*Pennsylvania State University, University Park, Pennsylvania 16802, USA*
[32]*Institute of High Energy Physics, Protvino, Russia*
[33]*Purdue University, West Lafayette, Indiana 47907, USA*
[34]*Pusan National University, Pusan, Republic of Korea*
[35]*University of Rajasthan, Jaipur 302004, India*
[36]*Rice University, Houston, Texas 77251, USA*
[37]*Universidade de Sao Paulo, Sao Paulo, Brazil*
[38]*University of Science & Technology of China, Hefei 230026, China*
[39]*Shandong University, Jinan, Shandong 250100, China*
[40]*Shanghai Institute of Applied Physics, Shanghai 201800, China*
[41]*SUBATECH, Nantes, France*
[42]*Texas A&M University, College Station, Texas 77843, USA*
[43]*University of Texas, Austin, Texas 78712, USA*
[44]*Tsinghua University, Beijing 100084, China*
[45]*United States Naval Academy, Annapolis, Maryland 21402, USA*
[46]*Valparaiso University, Valparaiso, Indiana 46383, USA*
[47]*Variable Energy Cyclotron Centre, Kolkata 700064, India*
[48]*Warsaw University of Technology, Warsaw, Poland*
[49]*University of Washington, Seattle, Washington 98195, USA*
[50]*Wayne State University, Detroit, Michigan 48201, USA*
[51]*Institute of Particle Physics, CCNU (HZNU), Wuhan 430079, China*
[52]*Yale University, New Haven, Connecticut 06520, USA*
[53]*University of Zagreb, Zagreb, HR-10002, Croatia*

---

[*]Deceased.

We report on a measurement of the $\Upsilon(1S + 2S + 3S) \rightarrow e^+ e^-$ cross section at midrapidity in $p + p$ collisions at $\sqrt{s} = 200$ GeV. We find the cross section to be $114 \pm 38(\text{stat} + \text{fit})^{+23}_{-24}(\text{syst})$ pb. Perturbative QCD calculations at next-to-leading order in the color evaporation model are in agreement with our measurement, while calculations in the color singlet model underestimate it by 2σ. Our result is consistent with the trend seen in world data as a function of the center-of-mass energy of the collision and extends the availability of Υ data to RHIC energies. The dielectron continuum in the invariant-mass range near the Υ is also studied to obtain a combined yield of $e^+ e^-$ pairs from the sum of the Drell-Yan process and b-$\bar{b}$ production.

I. INTRODUCTION

The main focus of the heavy flavor program at RHIC is to investigate the properties of the quark-gluon plasma (QGP) by studying its effect on open heavy flavor and quarkonia production. J/ψ suppression induced by Debye screening of the static quantum chromodynamics (QCD) potential between $c\bar{c}$ pairs was originally hailed as an unambiguous signature of QGP formation [1]. However, this simple picture is complicated by competing effects that either reduce the yield, such as comover absorption [2,3], or enhance it, such as in recombination models [4–6]. Recently, a growing interest in studying the Υ meson and its excited states has been kindled as it is expected that color screening will be the dominant effect contributing to any observed suppression of bottomonium production in heavy-ion collisions. A full spectroscopy of quarkonia states is now clearly recognized as one of the key measurements needed to understand the matter produced in high-energy heavy-ion collisions [7]. In particular, it has been recognized that data on the particle spectra of bottomonia can provide valuable information to constrain QGP models [8]. Because of the low production cross section of b-$\bar{b}$ at RHIC ($\sigma_{b\text{-}\bar{b}} \approx 1.9 \ \mu$b, [9]), recombination effects in $A + A$ collisions are negligible. At the same time, the interaction cross section of bottomonium with the abundantly produced hadrons in these collisions is small [10], so suppression due to absorption by hadronic comovers is expected by these models to be relatively unimportant. However, it will still be important to study Υ production in $d + $ Au collisions since available measurements by E772 [11] of cold nuclear matter effects on Υ production at lower energy show some suppression. Nevertheless, the amount of suppression seen for the Υ family is measured to be smaller than for charmonia. Therefore, bottomonium is expected to be a cleaner probe of high-temperature color screening effects.

In addition to its important role in establishing deconfinement, a measurement of the Υ 1S, 2S, and 3S states in $p + p$ and heavy-ion collisions can help to set limits on the medium temperature. The quarkonium measurements help in reaching these key goals because (i) an observation of

suppression of Υ production in heavy ions relative to $p + p$ would be a strong argument in support of Debye screening and therefore of deconfinement [12], and (ii) the sequential suppression pattern of the excited states is sensitive to the temperature reached in the medium [7]. In this regard, lattice QCD studies have seen a burst of activity in recent years. Studies of quarkonia spectral functions and potential models based on lattice QCD indicate that while the $\Upsilon(3S)$ melts even before the deconfinement transition and the $\Upsilon(2S)$ is likely to melt at RHIC ($\sqrt{s} = 200$ GeV), the $\Upsilon(1S)$ is expected to survive [7,13,14]. Recent results [12,15] indicate further that almost all quarkonia states [J/ψ, ψ', χ_c, χ_b, $\Upsilon(2S)$] melt below $1.3T_c$ and the only one to survive to higher temperature is the $\Upsilon(1S)$, which melts at $2T_c$, where $T_c \approx 175$ MeV is the critical temperature for the parton-hadron phase transition. Therefore, a systematic study of all quarkonia states in $p + p$, $d + $ Au, and Au $+$ Au collisions will provide a clearer understanding of the properties of the quark-gluon plasma.

Suppression of the $\Upsilon(2S)$ and $\Upsilon(3S)$ should be measurable at RHIC energies with increased integrated luminosity. In the near future, the larger luminosities proposed by the RHIC II program [16] will allow for a statistically significant measurement of all 3 states. With the objective of embarking in such a long program, one of the first steps is to establish a baseline cross section measurement of the bottomonia states in $p + p$ collisions. There are no previous measurements of Υ production in $p + p$ at the top RHIC energy for heavy ions (an upper limit was estimated in the 2004 data with only one-half of the calorimeter [17]). The luminosities available at RHIC in the 2006 run provided the first opportunity to measure bottomonium at the previously unexplored center-of-mass energy of $\sqrt{s} = 200$ GeV. A dedicated trigger algorithm exploiting the capabilities of the STAR electromagnetic calorimeter is essential for this measurement, and its development in STAR allows the Υ family to be studied in the $e^+ e^-$ decay channel. In this paper, we report our result for the $\Upsilon(1S + 2S + 3S)$ cross section at midrapidity, obtained with the STAR detector in $p + p$ collisions at $\sqrt{s} = 200$ GeV via

the e^+e^- decay channel. This measurement uses an integrated luminosity of 7.9 pb^{-1} collected during RHIC run VI (2006). We compare our data to perturbative QCD (pQCD) calculations done at next-to-leading order (NLO) in the color evaporation model (CEM) [16] and in the color singlet model (CSM) [18].

The article is organized as follows. Section II explains the detector setup. The details of the quarkonia triggers are explained in Sec. III. The acceptance and trigger efficiency are discussed in Sec. IV. After a detailed discussion of the data analysis procedure in Sec. V, we present our results and compare with pQCD calculations and with available data in Sec. VI. Our findings are summarized in Sec. VII.

II. DETECTOR OVERVIEW

The main detectors used in the STAR quarkonia program are the time projection chamber (TPC) [19], the barrel electromagnetic calorimeter (BEMC) [20], and the beam-beam counters (BBC) [21].

The BBCs are segmented scintillator rings covering the region $3.3 < |\eta| < 5.0$. The STAR $p + p$ minimum-bias trigger requires the coincidence of hits in the BBCs on opposite sides of the interaction region and is used to monitor the integrated luminosity for measuring absolute cross sections. The BBC acceptance and efficiency were studied previously [22], and it was found from simulations that for $p + p$ nonsingly diffractive (NSD) events the BBC trigger was $87 \pm 8\%$ efficient. The absolute $p + p$ cross section seen by the BBC trigger was measured via a van der Meer scan to be 26.1 ± 0.2 (stat) ± 1.8 (syst) mb.

The TPC and BEMC have a large acceptance at midrapidity: the single track coverage of the TPC + BEMC in pseudorapidity is $|\eta| < 1$ and complete in azimuth. The BEMC is divided in η and φ into 4800 towers. The size of each tower in $\eta \times \varphi$ is 0.05×0.05 rad. The geometrical acceptance of the STAR BEMC for detecting both electrons from an Υ decay is about $\approx 30\%$ over all phase space, and $\approx 60\%$ for Υ's in the kinematic range $|y| < 0.5$ and $p_\perp < 5$ GeV/c. We focus on this kinematic range, where the acceptance of the detector is optimal.

The capability of the TPC + BEMC for electron identification and the triggering capabilities of the BEMC are the two pillars of the STAR quarkonium program. In particular, the BEMC trigger allows us to sample the full luminosity delivered by RHIC to look for the high-mass dielectron signals characteristic of the $\Upsilon \rightarrow e^+e^-$ decay.

III. THE STAR QUARKONIA TRIGGERS

The STAR quarkonia trigger is a two-stage system comprising a level-0 (L0) hardware component [23] (decision time of $\approx 1 \mu$s) and a level-2 (L2) software component (decision time of $\approx 100 \mu$s in $p + p$, and $\approx 400 \mu$s in Au + Au). There were two separate Υ triggers used during the 2006 run; in the following we refer to them as trigger I

and trigger II. They were identical in concept, with the only difference being an increase in thresholds, which was necessary to reduce the trigger rate and reduce dead time while data taking. We discuss the triggers next and list all the parameters and thresholds. These were chosen based on simulations and on expected trigger rates based on calorimeter data taken in 2003.

A. Υ L0 trigger

The L0 trigger is a minimum-bias $p + p$ trigger with the additional requirement of signals in the BEMC consistent with a high-energy electron. The energy deposited in the calorimeter towers is measured by collecting scintillation light from the electromagnetic shower. The signal is digitized, pedestal subtracted, and sent to the L0 data storage and manipulation (DSM) hardware as a 6-bit analog-to-digital converter (ADC) value for triggering. The calorimeter calibration is done such that tower ADC values are proportional to deposited electromagnetic transverse energy ($E_\perp$), making it useful for triggering on high-$p_\perp$ electrons. The L0 trigger decision is made for every bunch crossing.

For the Υ analysis, the L0 decision was based on two quantities. The first is related to the signal in distinct towers. The tower with the highest $E_\perp$, as represented by the DSM-ADC value, is called the "high tower" (HT) in the event. The second quantity is a sum of towers in fixed η-φ regions of the BEMC, where each region comprises 4×4 towers. Each of these regions is named a "trigger patch" (TP). Since each tower covers 0.05 units in η and 0.05 rad in φ, the TP coverage is 0.2×0.2 rad. The L0 trigger is issued for trigger I (trigger II) if all of the following three conditions are met: (i) an event has a high tower with a DSM-ADC value >12 (16), corresponding to $E_\perp \approx 2.6$ (3.5) GeV deposited in the tower; (ii) the trigger patch containing the high tower has a total DSM-ADC sum over the 16 towers in the patch with a value >17 (19), corresponding to $E_\perp \approx 3.8$ (4.3) GeV, and (iii) the STAR $p + p$ minimum-bias trigger is met. The minimum-bias trigger is based on a BBC coincidence and is described elsewhere [22]. The coincidence of high-tower and trigger patch triggers will be referred to as "HTTP" in the remainder of the paper.

Figure 1 shows the $p_\perp$ distribution for simulated electrons and positrons from Υ decays in which both daughters are within the STAR acceptance. For each decay, we plot the $p_\perp$ distribution of the electron (filled circles) or positron (open squares) with the highest $p_\perp$ (the abscissa is simulated $p_\perp$). The electron and positron distributions are identical, as expected for a two-body decay into daughters with identical masses. The histogram in the figure is the sum, i.e., the $p_\perp$ distribution for the hardest of the two daughters. The corresponding DSM-ADC values used in the L0 trigger (which are proportional to $p_\perp$) are shown in Fig. 2. The L0 HT trigger II threshold of 16 is shown by the vertical dashed line.
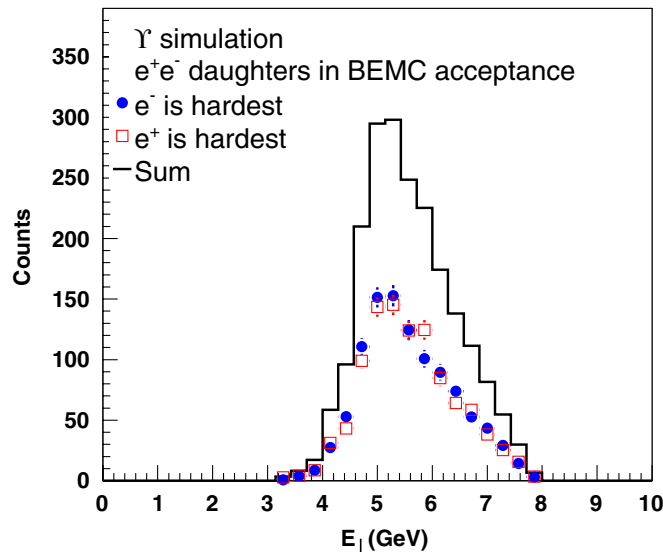
FIG. 1 (color online). The $E_\perp$ distribution for simulated ϒ daughter electron (filled circle) or positron (open square) with the highest $E_\perp$. We show only daughters that fall in the STAR BEMC geometrical acceptance. The histogram is the sum of the two distributions. The L0 HT trigger II threshold of 16 counts corresponds to $E_\perp \approx 3.5$ GeV.

From the $p_\perp$ and ADC distributions for the hardest ϒ daughter in Figs. 1 and 2, the average values are $\langle p_\perp \rangle = 5.6$ GeV/c and $\langle ADC \rangle = 18.0$ counts. Since the trigger threshold is placed at 16 ADC counts, the hardest daughter will typically fire the trigger. We find that 25% of the ϒ's produced at midrapidity have both daughters in the BEMC acceptance and at least one of them can fire the L0
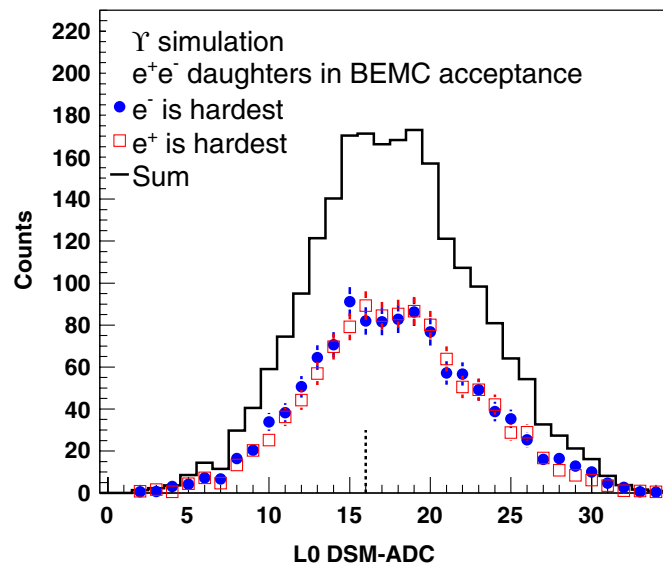

FIG. 2 (color online). The L0 DSM-ADC distribution for the electron (filled circle) or positron (open square) with the highest ADC. The histogram is the sum. The simulated ϒ is triggered when one of its daughter electrons is above the dashed line, which indicates the L0 HT trigger II threshold of 16 counts.

trigger. The details of the HTTP trigger efficiency and acceptance are discussed in Sec. IV.

B. ϒ L2 trigger

Once a L0 HTTP trigger is issued, the information for all detectors in STAR begins to be digitized. During this time, the L2 system can use the information from the 4800 individual calorimeter towers to decide whether to keep the event or to abort the readout. The L2 system can use the full energy resolution of the calorimeter (a 10-bit ADC value, in contrast to the 6-bit ADC used at L0). The L2 ϒ trigger makes the decision by looking for calorimeter signatures consistent with the production of a high invariant-mass electron-positron pair. (Since the L2 trigger uses BEMC information only and does not distinguish electrons from positrons, we will refer to electrons and positrons simply as "electrons" in all discussions of the L2 trigger.) At a minimum, one pair of candidate electrons is required. They are processed as follows. (We will denote kinematical quantities obtained in the L2 stage with the superscript "L2" to distinguish them from similar quantities obtained during the offline analysis.)

The algorithm starts by searching for all towers above the L0 high tower threshold. Each of these is treated as a seed for a 3-tower cluster. To produce the clusters, we search in the η-φ region around each high tower, with a search window of 3×3 towers. This area is smaller than the TP size in order to focus on electron finding, as our simulations show that electrons will likely have most of their energy contained in only 3 towers. We sort these 8 surrounding towers according to their measured energy and pick the two highest-$E_\perp$ towers in this list to produce a 3-tower cluster. This L2 tower clustering gives a better estimate of the electron energy compared to a single tower due to possible shower leakage into neighboring towers. If the energy of this 3-tower cluster is greater than 4.0 GeV it is considered for further processing, and we label such clusters as "L2 cluster-1."

We next look for additional electron candidates in the event. While it is possible for an event to have two towers above the HT threshold, the majority of events will have only one. We select additional electron candidates by starting with towers which have $E_\perp \gtrsim 0.7$ GeV (10-bit ADC of at least 75 counts after pedestal subtraction). Starting from these second seeds, we again construct 3-tower clusters (L2 cluster-2) using the procedure outlined above. We require that the L2 cluster-2 energy be $E_2^{L2} > 2.5$ GeV. After the complete iteration to find electron clusters, we make all possible cluster pairs (where each pair must have at least one L2 cluster-1) and calculate two pairwise quantities: the opening angle and the invariant mass of the pairs. These are calculated under the approximation that the vertex location is in the center of the detector and that the electrons travel in a straight line. Since the majority of the e^+e^- pairs from ϒ decays have

a large opening angle (θ), we look for pairs with $\cos(\theta_{12}^{L2}) < 0.5$, where θ_{12}^{L2} is the angle between the two clusters calculated in the L2 algorithm. With the combined information on the energy of the two clusters and their opening angle, we reconstruct the invariant mass via the approximate formula $M_{12}^{L2} \approx \sqrt{2E_1^{L2}E_2^{L2}(1 - \cos\theta_{12}^{L2})}$. We can neglect the electron mass of 0.511 MeV/c^2 as it would only contribute ≈ 1 MeV/c^2, which is small for ultrarelativistic electrons. For comparison, the straight-line approximation and the energy resolution result in a mass resolution of ≈ 900 MeV/c^2 as will be discussed in the following section. We select events with cluster-pair invariant masses in the range $6 < M_{12}^{L2} < 15$ GeV/c^2. If there is any pair that satisfies both of the pairwise conditions in the event, the algorithm issues an L2 trigger.

C. Trigger performance

In order to evaluate the trigger performance, we applied the trigger II cuts to the trigger I data. To do this, the exact same trigger condition was applied offline on the recorded values of the original trigger input data. Since events satisfying trigger II cuts also satisfy trigger I cuts, applying the tighter set of trigger II cuts to the trigger I data offline allows us to make a single data set with uniform properties for the entire 2006 run. The integrated luminosity for trigger I was $\mathcal{L} = 3.12 \pm 0.22$ (syst) pb^{-1}, and for trigger II it was $\mathcal{L} = 4.76 \pm 0.33$ (syst) pb^{-1}, giving a total integrated luminosity of 7.9 ± 0.6 pb^{-1}, where the 7% uncertainty originates from the uncertainty in the BBC measurement of the cross section as determined by a van der Meer scan [22].

Figure 3 shows the ADC distribution of the tower with the largest $E_\perp$ for each candidate pair seen at the trigger level in an event (in very few cases we find more than one tower above the L0 threshold, so most events have only one candidate pair). The two triggered data sets are shown, with trigger II displayed as squares and trigger I (after applying trigger II cuts) displayed as circles. The rejection factor achieved with trigger II, defined as the number of minimum-bias events counted by the trigger scalers divided by the number events where the trigger was issued, was found to be 1.8×10^5. The distributions seen at the trigger level only include information from the BEMC. This causes the trigger rate seen in the experiment to be dominated by background from dijet events with two nearly back-to-back π^0's. This dijet background is removed offline when including tracking information from the TPC. The trigger distributions are scaled by the overall luminosity in order to compare the relative normalization of the two data sets. The scale is chosen such that the counts in each triggered data set correspond to an integrated luminosity of 1 pb^{-1}. The relative luminosity normalization between the data sets agrees to a level of $\approx 1\%$. The solid-line histogram is from simulated $\Upsilon(1S)$ after
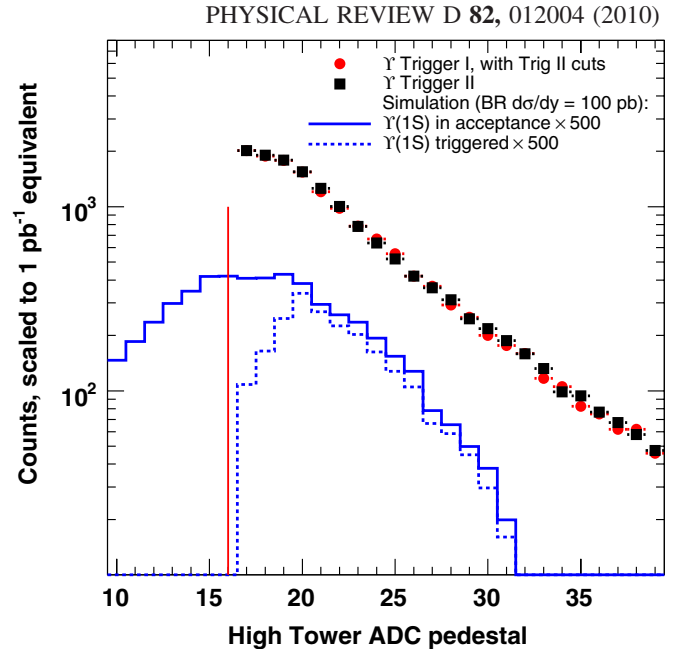
FIG. 3 (color online). The L0 DSM-ADC distribution ($\propto E_\perp$) for the highest EMC tower of a candidate pair. We show trigger I data after applying trigger II thresholds (red circles) and trigger II data (black squares). The yields are normalized by the integrated luminosity. The histograms are from simulation of $\Upsilon(1S)$, showing the corresponding distribution for electron daughters satisfying acceptance (solid line) and trigger (dotted line) requirements. The simulation histograms are normalized assuming $\mathcal{B} \times d\sigma/dy = 100$ pb, times a factor of 500 for clarity. The vertical line is the trigger II threshold of 16 counts. The histograms have the bin centers set at integer values to match the integer nature of ADC counts.

acceptance selection, requiring both electrons to deposit at least 1 GeV of energy in the BEMC. It shows the spectrum for the daughter with the highest ADC count. The spectrum for the simulated $\Upsilon(1S)$ events that satisfy all the trigger requirements is shown as the dashed-line histogram. The vertical line at 16 ADC counts represents the L0 ADC threshold for trigger II. In order to compare the size of the expected Υ signal relative to the trigger background from dijets, the histograms from the simulations for the $\Upsilon(1S)$ are scaled with two factors. The first factor corresponds to normalizing to an integrated luminosity of 1 pb^{-1} assuming a cross section times branching ratio into e^+e^- for the $\Upsilon(1S)$ at midrapidity of 100 pb, chosen because it is of the expected order of magnitude. From this, we expect 1υ every ≈ 3000 triggers, so we use a second multiplicative factor of 500 for display purposes. The spectral shape of the data in Fig. 3 is therefore dominated by dijet background. The same normalization and scale factors are used in Figs. 4–6 for comparing the trigger-level background distributions and the expected $\Upsilon(1S)$ signal.

Figure 4 shows the distribution of the L2 cluster-1 energy for all clusters that include a tower above the HT

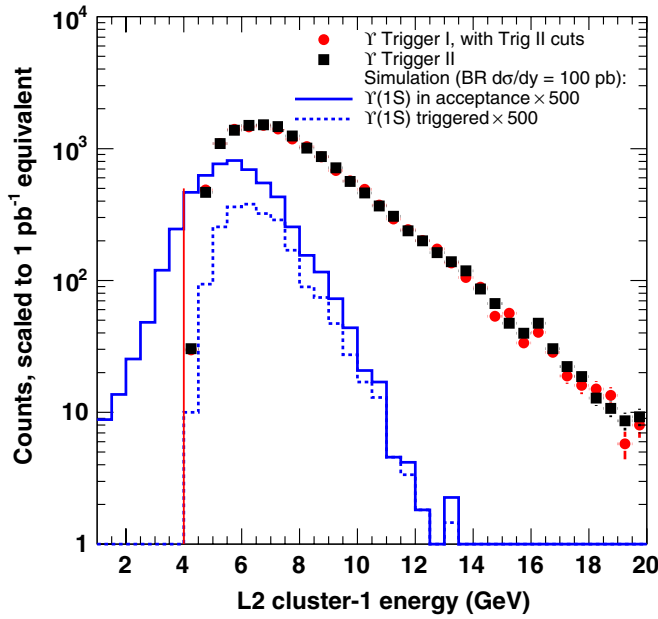FIG. 4 (color online). The distribution of L2 cluster-1 energy E_1^{L2} for all towers above the HT threshold in a trigger patch above the TP threshold. The L2 trigger requires $E_1^{L2} > 4.0$ GeV (vertical line). The line histograms show the ϒ (from simulation) after acceptance requirements (solid line), and after all trigger requirements (dashed line). The normalization and scaling factors are the same as in Fig. 3.

FIG. 5 (color online). The distribution of cosine of L2 opening angle θ_{12}^{L2} for accepted events. The line histograms show the ϒ distribution after acceptance requirements (solid line), and after all trigger requirements (dashed line). The vertical line shows the location of the trigger threshold. Normalization and scaling factors are the same as in Fig. 3.

DSM-ADC threshold of 16 ADC and that have their corresponding trigger patch DSM-ADC sum above the threshold of 19 ADC counts. It can be seen that the peak of the L2-cluster distribution near 6 GeV is not right at the threshold of 4 GeV (vertical line). This must happen because another trigger selection that is correlated to the measurement of the L2 cluster is being applied. In our case it is the L0 selection, which consists of both the HT and the TP requirement. Once we see a tower with energy above the HT threshold that is also in a trigger patch with energy above the TP threshold, the energy in the 3-tower cluster for that tower will likely already be above the L2 E1 threshold.

The distribution for the L2 opening angle θ_{12}^{L2} is shown in Fig. 5. It is highly peaked toward back-to-back topologies, much more so than the distribution from simulated ϒ's. This again reflects the fact that the triggered distribution is dominated by back-to-back π^0's. The majority of these are rejected offline when requiring the presence of a corresponding electron track in the TPC.

The L2 invariant-mass distribution shown in Fig. 6 is peaked at ≈ 8 GeV/c^2 due to the cluster energy requirements. The vertical lines depict the lower and upper thresholds at 6 and 15 GeV/c^2. The histogram shows the simulated ϒ(1S) before any trigger cuts (solid line) and after passing all the previous thresholds (dashed line). The trigger preferentially rejects lower L2-mass ϒ events, because these can happen when the energy clusters measured
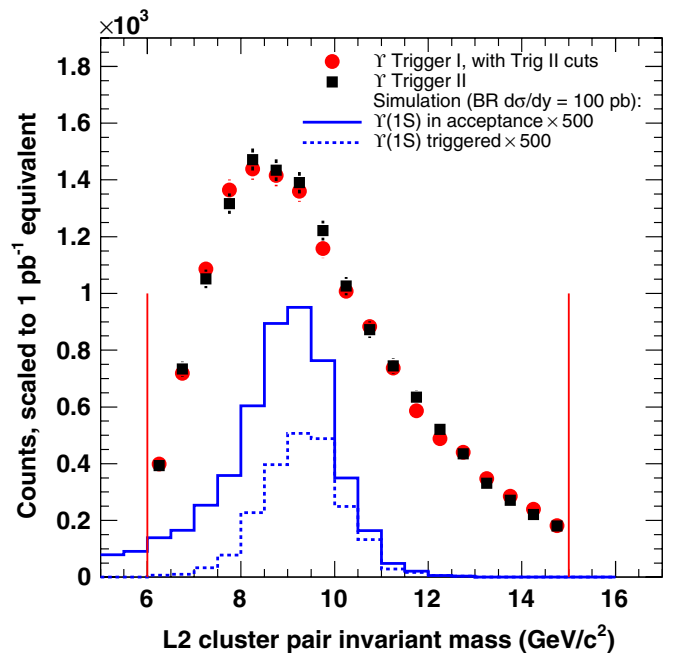
FIG. 6 (color online). The L2 invariant-mass M_{12}^{L2} distribution for accepted events. The line histograms show the ϒ M_{12}^{L2} distribution after acceptance requirements (solid line), and after all trigger requirements (L0 HTTP trigger, L2 cluster, L2 opening angle, and L2 invariant mass) of the e^+e^- daughters (dashed line). Vertical lines show location of the trigger thresholds. Normalization and scaling factors are the same as in Fig. 3.

in the calorimeter are lower than their average, and these clusters are preferentially rejected by the algorithm. From these simulations we estimate the Υ mass resolution of the L2 trigger to be 849 ± 8 MeV/c^2. It is dominated by the BEMC energy resolution and by the straight-line approximation used to calculate the opening angle in the L2 trigger algorithm. This is about an order of magnitude larger than the offline mass resolution, where the electron trajectories and momenta are obtained from tracking. Since all the Υ's that reach this stage are contained within the invariant-mass limits, this invariant-mass cut serves mainly to reject background.

In addition, the L2 information (such as that shown in Figs. 4–6) is available online after every run. These distributions serve as useful diagnostic tools during data taking.

IV. Υ ACCEPTANCE AND TRIGGER EFFICIENCY

To determine the geometrical acceptance of the detector for measuring $\Upsilon \rightarrow e^+e^-$, we combined two types of events in the following way. For the first type, we performed GEANT simulations of the $\Upsilon \rightarrow e^+e^-$ decays and propagated them through the detector geometry. The simulations were done with uniform population of the $p_\perp$-y phase space, folded with a Gaussian in y ($\sigma = 1$) and a realistic $p_\perp$ distribution. We chose the form $dN/dp_\perp \propto p_\perp/(\exp(p_\perp/T) + 1)$ with the parameter $T = 2.2$ GeV/c obtained from a fit to CDF data [24]. The dependence of the acceptance on the choice of $p_\perp$ distribution is negligible. This was verified by using functional forms derived from data at lower energy. Each simulated decay was combined with a simulated $p + p$ minimum-bias event using the PYTHIA event generator [25] with CDF tune A settings [26]. For the second type, we used a set of data collected by triggering on a RHIC bunch crossing. These were labeled "zero bias" as they do not require signals in any of the STAR detectors. These zero-bias events do not always have a collision in the given bunch crossing, but given that in the 2006 $p + p$ run the dominant contribution to the TPC occupancy was from pileup, these events will include the pileup from out-of-time collisions and all detector effects. When the zero-bias events are combined with simulated events, they provide the most realistic environment to study the detector efficiency and acceptance. Each PYTHIA + Υ event was embedded into a zero-bias event. The vertex position chosen for the simulated event was sampled from a realistic distribution of event vertex positions obtained from the Υ triggered data. With this procedure, we estimate both the trigger efficiency and the reconstruction efficiency (discussed in Sec. V).

For our purposes, a simulated Υ is considered to fall in the acceptance of the detector if each of its decay electrons deposits at least 1 GeV in a BEMC tower, as simulated by GEANT. We find that the acceptance depends strongly on the Υ rapidity (y_Υ), but weakly on its transverse momen-
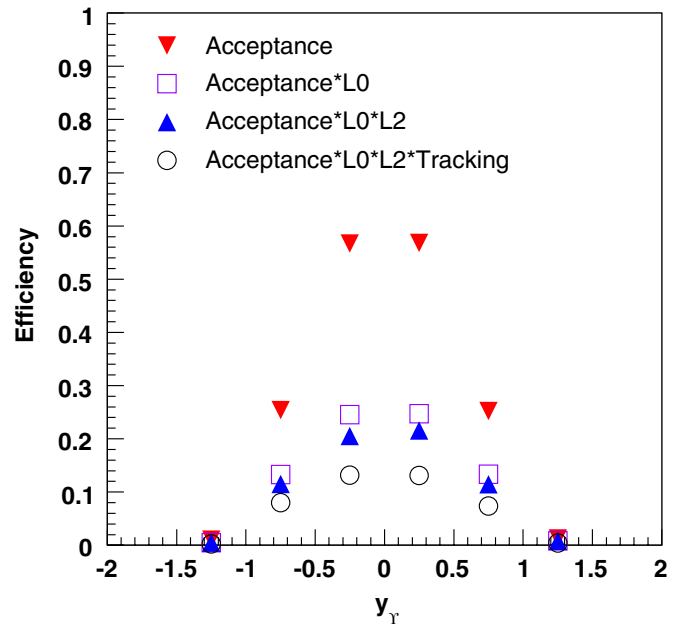

FIG. 7 (color online). Combined acceptance × efficiency as a function of rapidity y_Υ for the decay $\Upsilon \rightarrow e^+e^-$ in STAR. Down triangles: BEMC acceptance only; open squares: adding L0 requirement; upright triangles: adding L2 requirement; open circles: adding TPC acceptance + TPC tracking cuts and TPC-BEMC matching.

tum ($p_{\perp\Upsilon}$). At $|y_\Upsilon| < 0.5$ the acceptance is 57%, dropping to below 30% beyond $|y_\Upsilon| = 0.5$, and is close to zero beyond $|y_\Upsilon| = 1.0$. This is illustrated in Fig. 7, where the downward triangles depict the geometrical acceptance of the BEMC detector ϵ_{geo} obtained from the analysis of the simulated Υ decays in the real data events.

For those simulated Υ's that are accepted, we calculate the trigger efficiencies. This requires simulations of the BEMC response, digitization, and running the result through the offline reconstruction software chain. The HTTP requirement and the L2 trigger condition cut out an additional fraction of the events, and the combined acceptance and trigger efficiency is shown in Fig. 7. The squares include the effect of the HTTP trigger requirement ϵ_{L0} and the upright triangles include the L2 trigger condition ϵ_{L2}. The open circles include TPC acceptance plus

TABLE I. Acceptance, trigger efficiency, and tracking efficiency for reconstructing $\Upsilon \rightarrow e^+e^-$ in STAR in the kinematic region $|y_\Upsilon| < 0.5$. The first 4 rows are for the 1S and the last row is for the cross section–weighted 1S + 2S + 3S combination. All systematic uncertainties are listed in Table IV.

Quantity	Value
ϵ_{geo}	0.57
$\epsilon_{\mathrm{geo}} \times \epsilon_{\mathrm{L0}}$	0.25
$\epsilon_{\mathrm{geo}} \times \epsilon_{\mathrm{L0}} \times \epsilon_{\mathrm{L2}}$	0.21
$\epsilon_{\mathrm{geo}} \times \epsilon_{\mathrm{L0}} \times \epsilon_{\mathrm{L2}} \times \epsilon_{\mathrm{track}} \times \epsilon_R$	0.13
$\epsilon_{\mathrm{geo}} \times \epsilon_{\mathrm{L0}} \times \epsilon_{\mathrm{L2}} \times \epsilon_{\mathrm{track}} \times \epsilon_R$ (1S + 2S + 3S)	0.14

tracking efficiency ϵ_{track} and TPC-BEMC matching ϵ_R. These selections, as well as the particle identification cuts, are discussed in Sec. V. For the region $|y_\Upsilon| < 0.5$, the acceptance and efficiencies are given in Table I.

The relative systematic uncertainty on the L0 HT trigger efficiency was estimated to be $^{+5.9\%}_{-7.5\%}$ and is the dominant source of systematic uncertainty of the ϒ trigger efficiency. The systematic uncertainties for the L0 efficiency are asymmetric because the underlying $E_\perp$ distribution of the daughter electrons is not flat in the threshold region (see Fig. 3). A shift to a higher threshold reduces the yield more than a shift to a lower threshold increases it. The L0 HTTP trigger has a largest effect on the efficiency, as only 43% of the events in the acceptance remain after the trigger condition is applied. After including the L2 trigger, tracking, and TPC-BEMC matching efficiencies, we obtain a combined efficiency of 13.2% for the ϒ(1S).

A similar procedure was applied to the ϒ(2S) and ϒ(3S) states, which have slightly higher efficiencies due to their larger masses. We calculated a weighted average among the 3 states, including the branching ratio and the ratio of cross sections, in order to obtain an average efficiency to be applied to the measured yield of ϒ(1S + 2S + 3S). For this we use the branching ratios compiled by the PDG [27], and cross section ratios from NLO pQCD calculations in the CEM. The calculation used a bottom quark mass of $m_b = 4.75$ GeV/c^2, the parton distribution functions (PDFs) used are MRST HO [28], the choice of scale is $\mu = m_T$, and the center-of-mass energy is $\sqrt{s} = 200$ GeV [16]. The branching ratios and cross sections we used for this purpose are shown in Table II.

This procedure results in a combined acceptance, trigger efficiency, track finding efficiency, and TPC-BEMC matching efficiency of 14.3% for the averaged ϒ(1S + 2S + 3S) combination; see the last row of Table I. We estimate the sensitivity of the efficiency to the values in Table II in two ways. (i) By varying the branching ratio values by their uncertainty, we find that the efficiency varies in the range 14.2%–14.4%. (ii) Instead of using the numbers from Table II, we can use measured values of the ratios ϒ(2S)/ϒ(1S) and ϒ(3S)/ϒ(1S) from Ref. [29]. No further input is needed because the weighted average of the efficiency does not depend on the overall scale of the cross section: it cancels out when averaging. By varying these measured ratios within their uncertainty we obtain weighted efficiencies in the range 14.1%–14.4%. There-

fore, our results do not depend strongly on the values in Table II. In particular, the overall scale of the cross section from the NLO calculations has no direct impact on our results. Additional analysis cuts related to electron identification are discussed in the following section.

With thresholds of ≈ 4 GeV, the hadron rejection power of the BEMC towers at the energy relevant for ϒ decay daughters is $e/h \approx 100$. The main source of background for the trigger comes from high-$p_\perp$ π^0's decaying into two photons that deposit energy in the BEMC. The BEMC will therefore trigger on two high-$p_\perp$ π^0's with a large opening angle. These events are typically from dijets. Since these are also produced by large-momentum-transfer events with low cross section, the trigger rate is sufficiently small, even in the presence of this background, that the ϒ trigger can sample all collision events and is limited only by luminosity. The triggered distributions shown in Figs. 3–6 are dominated by the π^0 photon background. These background events are rejected in the offline analysis.

V. ϒ ANALYSIS

During the offline analysis, we use a complete emulation of the trigger to obtain all candidate BEMC tower pairs for an event. We use the TPC to select charged tracks and require that they point close in η-φ to the position of the candidate clusters. The TPC also allows us to obtain improved electron kinematics compared to those derived from BEMC information available at the trigger level and to perform particle identification via specific ionization. The matching of TPC tracks to BEMC clusters is also useful for electron identification via the ratio E/p.

Tracks are selected based on the number of TPC points found during the track pattern recognition and used in the fit to obtain the track kinematic parameters. The TPC tracks can have a maximum of up to 45 space points. We require that all tracks have at least 52% of their maximum possible points, and a minimum of 20 points. The first requirement guarantees we have no split tracks, and the second requirement sets a floor for those tracks which have a number of points smaller than 45 due to passing through inactive areas of the detector. We select tracks with $p_\perp > 0.2$ GeV/c to reject most low momentum tracks in a first pass. We do not impose higher $p_\perp$ requirements in the track selection stage because we also require E/p matching with the BEMC, where $E > 2.5$ GeV, as discussed below. Tracks are also required to extrapolate back to a primary vertex found in the event. We find the combined TPC acceptance times tracking efficiency for detecting each ϒ daughter to be $\epsilon_{\text{TPC}} = 85\%$, and to be approximately independent of electron $p_\perp$. Hence, the pairwise efficiency can be obtained by squaring the single-particle efficiency.

In order to guarantee that the analysis only uses tracks that could have fired the trigger, we impose a requirement that the tracks extrapolate close to the BEMC candidate

TABLE II. Branching fractions for ϒ(nS) → e^+e^- [27] and total cross sections at $\sqrt{s} = 200$ GeV from an NLO CEM model [16]. See text for details.

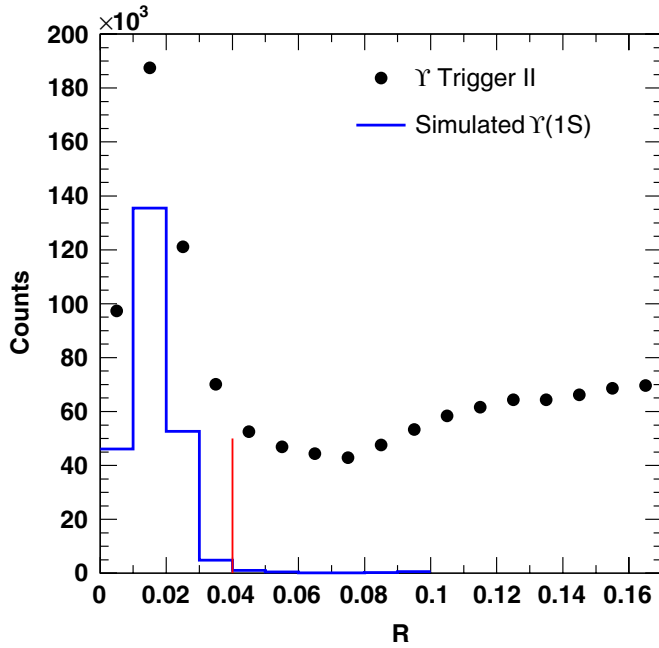| ϒ state	$\mathcal{B}$ (%)	σ (nb)
ϒ(1S)	2.38 ± 0.11	6.60
ϒ(2S)	1.91 ± 0.16	2.18
ϒ(3S)	2.18 ± 0.21	1.32

FIG. 8 (color online). The radial distance $R = \sqrt{\Delta\eta^2 + \Delta\varphi^2}$ between the TPC track and the EMC electron cluster for simulated Υ daughters (line histogram, arbitrary scale), and the R distribution from data (circles). We reject candidate tracks with $R > 0.04$ (vertical line).

towers. The requirement used was for them to be within a circle of radius $R < 0.04$ in η-φ space of the L2 candidate clusters. We find that this cut has an efficiency of $\epsilon_R = 93\%$ for a given Υ daughter electron, and has good background rejection power. This is illustrated in Fig. 8, which shows the R distribution for simulated $\Upsilon(1S)$ daughters as the line histogram. The R distribution from tracks passing basic quality cuts in the triggered events is shown as the solid circles.

An important component of the analysis is the vertex-finding efficiency. We find that in contrast to minimum-bias $p + p$ events, the Υ triggered events have a very high vertex-finding efficiency. The analysis benefits from the presence of the HT trigger, since these events are likely to have a high-$p_\perp$ track that facilitates the task of finding the vertex. We find that the vertex-finding efficiency ϵ_{vertex} for Υ events is $96.4 \pm 0.9\%$.

In the 2006 run, the luminosity was high enough that there can be multiple primary vertices due to pileup events in the TPC. We find that about $\approx 9\%$ of the Υ-triggered events have 2 or more vertices. For this analysis, we searched for candidates from all the vertices found in an event. We chose the vertex by requiring that the vertex also matched the high momentum TPC tracks that were already selected based on the BEMC tower extrapolation. Since the BEMC is read out after every bunch crossing, out-of-bunch pileup (interactions that happen before or after the triggered bunch crossing) is rejected by the TPC track–BEMC cluster matching requirement. We end up with a

unique, unambiguous vertex in all events. Within-bunch pileup (multiple interactions in the same bunch crossing) is negligible for this analysis. Pileup rejection will become more important as the luminosity of RHIC is increased.

Electrons were identified by selecting charged particle tracks with specific ionization energy loss dE/dx in the TPC consistent with the ionization expected for electrons. In the momentum region of interest ($p \gtrsim 3$ GeV/c), there is overlap between electrons and charged pions, so a cut was placed that yielded an electron efficiency of $\epsilon_{dE/dx} = 84\%$. The cut was chosen to optimize the effective signal S_{eff} of single electrons, $S_{\text{eff}} = S/(2B/S + 1)$, where S is the electron signal and B is the hadron background. To do this, we construct a normal distribution of ionization measurements. We use the measured ionization of each track, compare it to the expected ionization for an electron, and divide by the expected dE/dx resolution (which depends on the track length and number of measurements). This yields a normalized Gaussian distribution of ionization measurements, $n\sigma_{dE/dx}$. We fit this distribution with one Gaussian function to represent the electrons signal S, and two Gaussian functions to model the background B from pions and other hadrons.

In addition, we used the combined information of the EMC energy E, as obtained by the 3-tower candidate clusters from L2, and the TPC track momentum p to compute the E/p ratio, which should be unity for ultra-

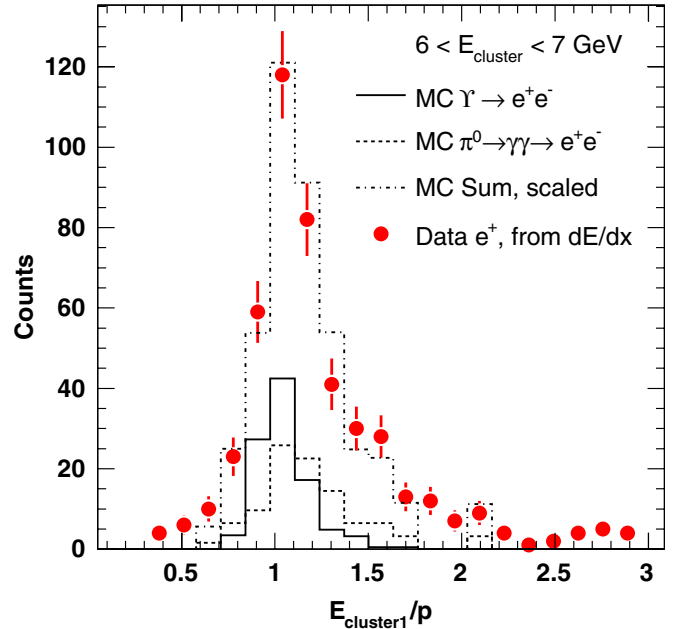FIG. 9 (color online). E/p distribution from Υ-triggered data events, selecting a high-purity sample of positrons via dE/dx (filled circles). We compare this to simulations from reconstructed e^+ and e^- from Υ decays (solid line) and from π^0 events where the decay photons produce a conversion e^+e^- pair (dashed line). The scaled sum of these two contributions is shown as the dot-dashed line.

relativistic electrons to a very good approximation. Figure 9 shows the E/p distribution comparison from an electron sample obtained from the trigger I and trigger II data sets (filled circles). Cuts were placed at $E/p = 1.0 \pm 0.3$, which is close to a 2σ cut, given that fitting with a Gaussian gives $\sigma = 0.157 \pm 0.002$. A shape that is approximately Gaussian is expected for the E/p distribution due to the Gaussian shape of the resolution in both the energy measurement done in the BEMC and in the curvature measurement done in the TPC (curvature is proportional to $1/p_\perp$). We see that the E/p distribution in the data shows a non-Gaussian tail. We studied the shape in several ways. To rule out distortions from misidentification of hadrons, we show only positrons to avoid any antiproton contamination and use tight dE/dx cuts to select only a very high-purity electron sample. We studied the energy dependence (to rule out threshold effects near 4 and 2.5 GeV), isolation cuts on the electron tracks (to rule out contamination of the BEMC energy measurement from nearby charged particles), and the E/p shape of embedded electrons and photons. We conclude that the tail at high E/p has two sources:

(1) Electron bremsstrahlung: The solid line in Fig. 9 shows the simulated E/p for ϒ electrons combined with a PYTHIA underlying $p + p$ event, embedded into zero-bias-triggered events. Many of these produce a Gaussian E/p distribution, but we also see a tail. By selecting simulated electrons which undergo bremsstrahlung, we find cases in which the Monte Carlo momentum at the outermost TPC point differs from the momentum at the ϒ decay vertex by more than 100 MeV/c. We then look at the E/p of these electrons, and find that their mean is shifted. All entries in the region $E/p \approx 1.3$ of the solid line in Fig. 9 come from these cases. Therefore, part of the non-Gaussian shape seen in the data is accounted for by electron bremsstrahlung in the detector material and is included in the distribution of simulated ϒ daughters.

(2) Photon conversions: Events with a high-Q^2 dijet that include back-to-back π^0's also fire the ϒ trigger. Some of the π^0 daughter photons will convert into e^+e^- pairs and leave a TPC track pointing at the EMC cluster. Generally, the e^+ and e^- will strike the calorimeter near the sibling photon, resulting in a track with a high E/p value. We analyzed these simulated π^0 events and applied the same tracking cuts, calorimeter clustering, and BEMC-TPC matching used in this paper to the resulting electrons. The E/p distribution for the electrons in these simulated events is shown as the dashed line in Fig. 9, and we see a non-Gaussian tail extending to larger values than that of the ϒ electrons. The average E/p for the electrons from π^0 events is ≈ 1.18 compared to ≈ 1.08 for ϒ electrons.

Of these two effects, the first needs to be taken into account in the ϒ efficiency because the ϒ daughters which undergo bremsstrahlung and have a resulting E/p value outside our cut will be removed from the analysis. The second effect does not need to be included in the E/p efficiency since it is not due to bottomonium events. These π^0-γ-conversion events will appear in the invariant-mass distributions, but they can be subtracted as follows. A single photon conversion produces an unlike-sign pair. When there are multiple photon conversions in an event, the combinations that can be made include unlike-sign and like-sign electron pairs. The unlike-sign pairs from a real photon will have zero invariant mass and do not affect the analysis. The additional unlike-sign combinatorial pairs will have a distribution that can be modeled by the like-sign combinations and are therefore removed when subtracting the like-sign pair combinatorial background.

Since the E/p distribution in the ϒ-triggered data set has both types of events, we reproduce the shape of the data using the two types of electron simulations: the electron E/p distributions from ϒ events (including the bremsstrahlung tail) and from π^0 events. These are added and scaled to approximately fit the data in the region $0.6 < E/p < 1.7$, shown as the dot-dashed line in Fig. 9.

As discussed above, we need to determine the efficiency for electrons only from ϒ sources. To do this, we use the ϒ embedding simulations to estimate the efficiency of our E/p cut, which includes both the Gaussian shape expected from detector resolution and the non-Gaussian tail due to bremsstrahlung. The systematic uncertainty in the determination of the E/p cut efficiency is dominated by the uncertainty in the knowledge of the detector material (and hence on the amount of bremsstrahlung), which was estimated to be a factor of 2. The material uncertainty is different from that quoted in previous STAR electron analyses because in this paper we do not restrict the event vertex to be near the center of the detector, where the material budget is lower and is better known. To estimate the uncertainty in the E/p cut efficiency, we construct an E/p distribution by splitting the original embedding simulation sample into electrons that undergo bremsstrahlung and electrons that do not. We scale the number of those that do by a factor of 2 and sum the two distributions to obtain a new E/p distribution. The estimated efficiency found in the bremsstrahlung-augmented distribution is lower by $\approx 3\%$, which we assign as the systematic uncertainty of $\epsilon_{E/p}$. All the efficiencies used to obtain the ϒ cross section and their systematic uncertainties are collected in Table IV.

VI. RESULTS AND DISCUSSION

Once we have tracks that satisfy our criteria and are matched to tower clusters that satisfy all the L0 and L2 trigger requirements, we form electron-positron pairs to produce the invariant-mass spectrum, using electron track momenta reconstructed in the TPC. We use the like-sign
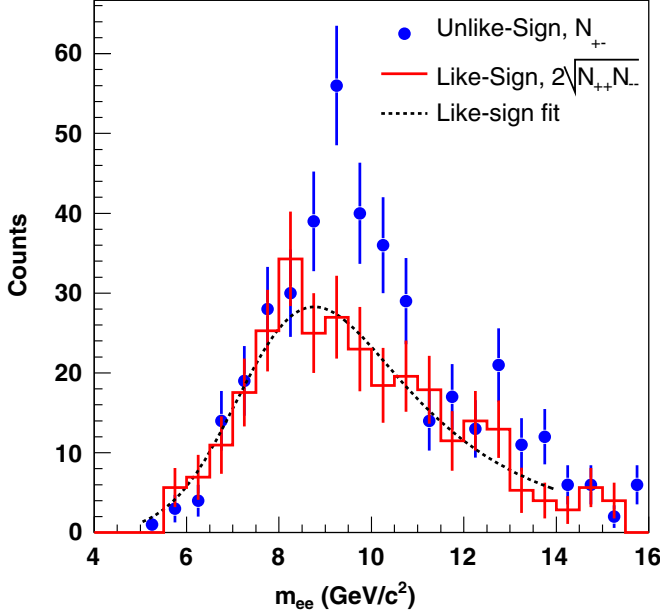
FIG. 10 (color online). Unlike-sign raw yield N_{+-} (filled circles) in the region $|y_{ee}| < 0.5$, where y_{ee} is the pairwise rapidity, and like-sign combinatorial background $2\sqrt{N_{++}N_{--}}$ (line histogram). The background is fit to an exponential multiplied with an error function representing the turn-on of the STAR Υ trigger (dashed line).

combinations of e^+e^+ and e^-e^- to estimate the combinatorial background (see e.g. [30]) via

$$N_{+-}^{\text{bck}} = 2\sqrt{N_{++}N_{--}} \cdot \frac{A_{+-}}{\sqrt{A_{++}A_{--}}}, \qquad (1)$$

where N_{+-} denotes the unlike-sign pair differential invariant-mass distribution dN_{+-}/dm and A_{+-} denotes the acceptance for unlike-sign pairs (similarly for the like-sign distributions). The symmetry of the BEMC and TPC for accepting unlike-sign and like-sign pairs makes the ratio of acceptances unity, so we only use $2\sqrt{N_{++}N_{--}}$ for the combinatorial background. The unlike-sign and like-sign background invariant-mass spectra are shown in Fig. 10.

A. Υ line shape

In this analysis, we cannot resolve individual states of the Υ family due to the limited statistics, finite momentum resolution, and electron bremsstrahlung resulting from the large material budget during the 2006 run. Therefore, the yield reported here is for the combined $\Upsilon(1S + 2S + 3S)$ states. The total dielectron unlike-sign yield after like-sign background subtraction has three contributions:

(1) The Υ states.
(2) The Drell-Yan continuum.
(3) The b-$\bar{b}$ continuum.

In order to separate these three contributions, we obtain

parametrizations for the expected shapes of each of the three components of the dielectron unlike-sign yield. The contribution from the Υ states is obtained by the same simulations that were used to obtain the detector efficiency. The reconstructed invariant-mass shapes for the 1S, 2S, and 3S states are individually obtained. Each of the shapes from the simulation is fit with a functional form introduced by the Crystal Ball experiment [31], which can accommodate detector resolution and losses due to bremsstrahlung in the detector material, and has the form:

$$f(m) = N \cdot \begin{cases} \exp\left(-\frac{(m-\mu)^2}{2\sigma^2}\right), & \text{for } \frac{m-\mu}{\sigma} > -\alpha, \\ A \cdot \left(B - \frac{m-\mu}{\sigma}\right)^{-n}, & \text{for } \frac{m-\mu}{\sigma} \leq -\alpha. \end{cases} \quad (2)$$

Requiring that the function and its derivative be continuous constrains the constants A and B to be

$$A = \left(\frac{n}{|\alpha|}\right)^n \cdot \exp\left(-\frac{|\alpha|^2}{2}\right), \qquad B = \frac{n}{|\alpha|} - |\alpha|. \quad (3)$$

We fix the parameters of the three Crystal Ball functions representing the three Υ states and then adjust the relative scales according to the average branching ratios and according to the ratios of cross sections shown in Table II. The overall integral of the Crystal Ball functions combined this way is left as a free parameter in the fit, which allows us to obtain the Υ yield.
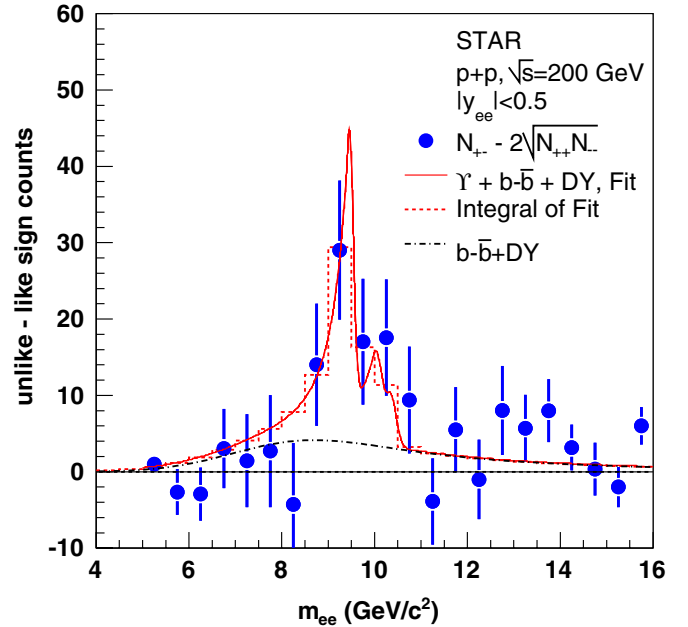
FIG. 11 (color online). The e^+e^- signal after subtracting the like-sign combinatorial background. The solid line is the function used to fit the data, composed of (a) three Crystal Ball functions [Eq. (2)] that represent the combined $\Upsilon(1S + 2S + 3S)$ line shape, (b) the Drell-Yan, and (c) the b-$\bar{b}$ contributions. We fit the data using the integral of the fit function in each mass bin, shown by the dashed-line histogram. The sum of the two continuum contributions is shown by the dot-dashed line. The integral of the Crystal Ball functions provides the net Υ yield.

Figure 11 shows the data used to obtain the ϒ and continuum yields. The data points are the unlike-sign e^+e^- signal after subtracting the like-sign combinatorial background. The background subtraction is done bin by bin. The error bars shown are statistical. The fit includes the contributions from the ϒ(1S + 2S + 3S) states and the continuum contributions from Drell-Yan and b-$\bar{b}$ shown as the solid-line function. The ϒ states are modeled with Eq. (2) to account for detector resolution and for losses due to bremsstrahlung which result in a tail to low values of invariant mass. The fit is done using the integral of the fit function in each bin, and is shown as the dashed-line histogram. We discuss next the procedure used to extract the continuum contributions (dot-dashed line) and the ϒ(1S + 2S + 3S) yield.

B. Drell-Yan and b-$\bar{b}$ continuum contributions

The Drell-Yan continuum is parametrized from a pQCD NLO calculation [32] done in the kinematic range $|y_{ee}| < 0.5$ and $m_{ee} > 4$ GeV/c^2. We convolute the calculated spectrum with the detector resolution (accounting for bremsstrahlung), but this introduces very small changes in the shape of the spectrum. We find that the shape of the Drell-Yan continuum is well described by a function of the form

$$\frac{A}{(1 + m/m_0)^n} \tag{4}$$

with the parameters $m_0 = 2.70$ GeV/c^2 and $n = 4.59$.

The b-$\bar{b}$ contribution is parametrized from a simulation using PYTHIA 8 [25]. We turn on production of b-$\bar{b}$ pairs and follow their fragmentation and subsequent decays of the B hadrons to look for dielectrons originating from the b quarks. We convolute the simulated shape with the detector resolution and bremsstrahlung and find that the shape is well described by a function of the form

$$\frac{A m^b}{(1 + m/m_0)^c} \tag{5}$$

with the parameters $b = 1.59$, $m_0 = 29.7$ GeV/c^2, and $c = 26.6$.

Since the STAR ϒ trigger is meant to reject events with low invariant mass, we parametrize the trigger response on both continuum contributions by multiplying them with an error function

$$\frac{\text{erf}((m - m_{\text{trig}})/w) + 1}{2}, \tag{6}$$

where m_{trig} is related to the trigger thresholds and w describes the width of the turn-on of the error function due to finite detector resolution. We obtain the parameters from the like-sign data (Fig. 10) by multiplying the error function with an exponential $\exp(-m/T)$ to account for the random like-sign combinations at higher mass. We use the like-sign data since the trigger turn-on shape for like-

sign and unlike-sign pairs is the same in our detector, but the like-sign invariant-mass distribution is purely due to combinatorics and can be fit with the simple parametrization given above (Fig. 10, dashed line). The parameters are $m_{\text{trig}} = 8.1 \pm 0.8$ GeV/c^2 and $w = 1.8 \pm 0.5$ GeV/c^2. A variation of the turn-on function parameters gave a negligible variation on the extracted yields, so it was not deemed necessary to estimate the trigger response on the continuum via a simulation. (We did use a simulation of the trigger response on simulated ϒ decays; see Fig. 6, dashed histogram.)

To obtain the ϒ yields and cross section, we perform a fit of the unlike-sign invariant-mass distribution after subtracting the like-sign background including contributions for the ϒ(1S + 2S + 3S), and the continuum due to Drell-Yan and b-$\bar{b}$ cross sections. Since the extracted ϒ yield from the fit will be sensitive to the continuum yield, we next discuss the effect that variations of the Drell-Yan and b-$\bar{b}$ cross sections can have on our result.

We find that the resulting shapes of the two continuum contributions are very similar. We can fit the continuum yield using the parametrized Drell-Yan and b-$\bar{b}$ contributions. The 1- and 2-σ contours in the 2D parameter space $\sigma_{b\text{-}\bar{b}}$ vs σ_{DY} are shown in Fig. 12, where the cross sections quoted are corrected for efficiency and acceptance and measured in the phase space region $|y| < 0.5$ and $8 < m_{ee} < 11$ GeV/c^2.

The fit shows a strong anticorrelation between the Drell-Yan and the b-$\bar{b}$ cross sections due to the similarity of the parametrized shapes. The Drell-Yan cross section spectral shape is slightly favored by our data, and we obtain the
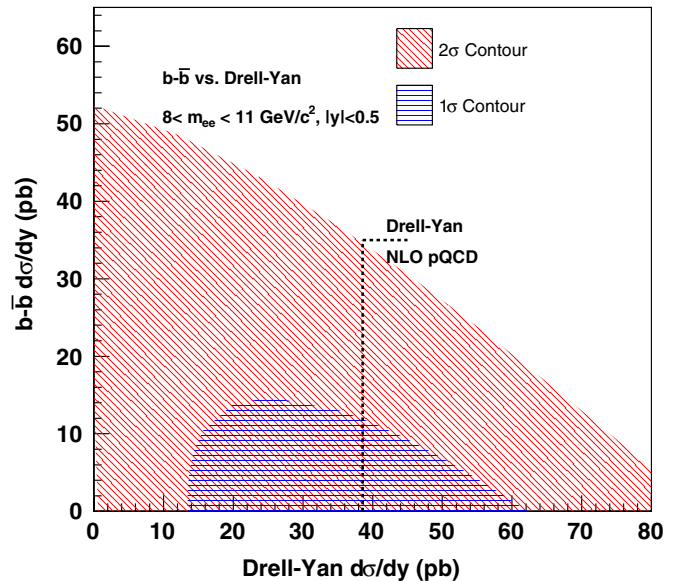

FIG. 12 (color online). The 1-σ (horizontal lines) and 2-σ (diagonal lines) contours obtained by fitting the data, showing the favored regions for the Drell-Yan and b-$\bar{b}$ cross sections. The dashed line shows the prediction for the Drell-Yan cross section from a pQCD NLO calculation [32].

minimal χ^2 for a Drell-Yan cross section of ≈ 38 pb with a negligible b-$\bar{b}$ contribution. The fit gives $\chi^2/\text{NDF} = 1.1$. The prediction from an NLO calculation of the Drell-Yan cross section [32] is shown as the vertical line at 38.6 pb and is consistent with values in the 1-σ region (horizontal lines). Our data also allow values of the b-$\bar{b}$ cross section up to ≈ 15 pb within the 1-σ range, provided the Drell-Yan yield is reduced. Given the anticorrelation, our data are mainly sensitive to the sum of the two cross sections, and within the 1-σ contour the allowed range for the sum of cross sections is $(\sigma_{\text{DY}} + \sigma_{b\text{-}\bar{b}})|_{|y|<0.5,\ 8<m<11\ \text{GeV}/c^2} = 38 \pm 24$ pb. This variation is taken into account in the fit to extract the Υ yield and is included in the quoted uncertainty.

C. Υ yield and cross section

The fitting function in Fig. 11 includes a total of three free parameters: the Υ yield, the Drell-Yan yield, and the b-$\bar{b}$ yield. This allows us to extract the Υ yield directly, automatically including (i) the statistical uncertainty for each mass bin in Fig. 11, and (ii) the uncertainty due to the anticorrelation between the continuum contributions and the Υ contribution. To compare the yield extraction using a different method, one can also perform bin counting. There are two ways to do this. One method is to take the background-subtracted unlike-sign yield directly from the data shown in Fig. 11, where the background subtraction is done for each mass bin. We then sum the resulting histogram in the mass region of the Υ peak, 8–11 GeV/c^2. This sum includes the Υ yield and the continuum contribution, so we subtract from it the contribution from the Drell-Yan and b-$\bar{b}$ continuum obtained in the fit. A second method is to sum the yield of the unlike sign (N_{+-}) in the region 8–11 GeV/c^2, do the same for the like-sign positive (N_{++}), and like-sign negative (N_{--}), and then do the subtraction $N_{+-} - 2\sqrt{N_{++}N_{--}}$. In other words, in the first method we do the subtraction bin by bin and then do the sum, in the second method we do the sum first to get a single bin and then we do the subtraction. The results for estimating $N_{+-} - 2\sqrt{N_{++}N_{--}}$ from the combined fit, the

TABLE III. Extraction of $\Upsilon(1S + 2S + 3S)$ yield by bin counting and fitting. The sums are done in the range $8 < m < 11$ GeV/c^2.

Fitting results	
$N_{+-} - 2\sqrt{N_{++}N_{--}}$	80.9
Υ counts	59 ± 20
Bin-by-bin counting	
$N_{+-} - 2\sqrt{N_{++}N_{--}}$	82.7
Υ counts	61 ± 20
Single-bin counting	
$N_{+-} - 2\sqrt{N_{++}N_{--}}$	75 ± 20
Υ counts	54 ± 18

bin-by-bin counting method, and the single-bin counting method, are shown in Table III.

The quoted uncertainty in $N_{+-} - 2\sqrt{N_{++}N_{--}}$ is listed for the single-bin counting method, which is obtained from a straightforward application of the statistical errors of the corresponding yields ($N_{+-} = 230$, $N_{++} = 92$, $N_{--} = 65$). It amounts to a contribution of 26% to the uncertainty and originates only from counting statistics. In addition to this purely statistical uncertainty, we must also take into account the uncertainty of the continuum subtraction. This part of the uncertainty is obtained from the fitting method in all the quoted Υ counts in the table. It should be noted that one cannot use counting statistics to estimate the uncertainty on the Υ yield due to the continuum subtraction. The reason is that the Υ and continuum yields are obtained from the same data, namely, the invariant-mass dielectron spectrum in Fig. 11. The two yields are therefore anticorrelated: a larger continuum yield reduces the extracted Υ counts. One must take this anticorrelation into account in the estimation of the uncertainty on the Υ yield. The best way to do this is to use the fitting method. In the fit, both the statistical precision of the invariant-mass spectrum and the anticorrelation between the Υ and continuum yields in the estimation of the uncertainty are taken into account when varying the Υ yield and the continuum yield to minimize the χ^2. We find the uncertainty from the fit to be 33% of the Υ yield, and we hence use this fitting-method result to estimate the uncertainty in all the Υ yields quoted in Table III. We quote this as the "stat + fit" uncertainty in our cross section result. It should be noted that with the statistics of the present analysis, we find that the allowed range of variation of the continuum yield in the fit is still dominated by the statistical error bars of the invariant-mass distribution, and so the size of the 33% uncertainty is mainly statistical in nature. However, we prefer to denote the uncertainty as stat + fit to clarify that it includes the estimate of the anticorrelation between the Υ and continuum yields obtained by the fitting method. A systematic uncertainty due to the continuum subtraction can be estimated by varying the model used to produce the continuum contribution from b-$\bar{b}$, e.g. LO vs NLO. The statistics in the dielectron invariant-mass distribution are such that the variation in the shape of the b-$\bar{b}$ continuum between LO and NLO would not contribute a significant variation to the Υ yield. This can be seen in Fig. 12, where the fit of the continuum allows for a removal of the b-$\bar{b}$ yield entirely, as long as the Drell-Yan contribution is kept. In this analysis, systematic variations of the models used to represent the continuum yields produce a negligible change in the extracted Υ yield with the current statistics.

When comparing different counting methods in Table III, we see that the difference between the bin-by-bin counting method and the fitting method is negligible. The single-bin counting method yield is lower than the one from the bin-by-bin counting method by 9%, and we assign this as a component of the systematic uncertainty.

Table III also lists the yield of Υ(1S + 2S + 3S). In the fitting method, the yield and the quoted uncertainty is obtained directly from the fit, as well as the contribution from Drell-Yan and b-$\bar{b}$ discussed in the previous section. This has the advantage that the uncertainty due to the continuum subtraction and the correlations between the Υ, Drell-Yan, and b-$\bar{b}$ contributions are automatically taken into account when exploring the parameter space. The disadvantage is that there is a model dependence on the line shapes used for the fit. In the counting methods, to extract the Υ yield we subtract the continuum contribution obtained from the fit. This reduces the model dependence on the Υ line shape. However, we must still account for the uncertainty in the estimate of the continuum contribution in the determination of the Υ yield uncertainty. Since this uncertainty should include similar correlations between the Υ yield and continuum yields as found in the fitting method, the relative uncertainties should be approximately equal. Therefore, we use the same relative Υ yield uncertainty for the counting methods as for the fitting method. To get the total Υ yield we must correct the above numbers for the yield outside the integration region. This correction can be obtained from the fitted Crystal Ball functions, and gives an additional 9% contribution to the Υ yield. We report results for the cross section using the bin-by-bin counting method.

In order to transform the measured yield of Υ(1S + 2S + 3S) into a cross section, we applied several correction factors:

$$\sum_{n=1}^{3} \mathcal{B}(nS) \times \sigma(nS) = \frac{N}{\Delta y \times \epsilon \times \mathcal{L}}, \qquad (7)$$

where the symbols are as follows. $\mathcal{B}(nS)$ is the branching fraction for $\Upsilon(nS) \to e^+ e^-$. $\sigma(nS)$ is the cross section $d\sigma/dy$ for the nS state in the region $|y_\Upsilon| < 0.5$. $N = 67 \pm 22$ (stat) is the measured Υ(1S + 2S + 3S) yield from the bin-by-bin counting method in Table III with a 9% correction to account for the yield outside $8 < m_{ee} < 11$ GeV/c^2. $\Delta y = 1.0$ is the rapidity interval for our kinematic region $|y_\Upsilon| < 0.5$. The total efficiency for reconstructing members of the Υ family is the product $\epsilon = \epsilon_{\text{geo}} \times \epsilon_{\text{vertex}} \times \epsilon_{\text{L0}} \times \epsilon_{\text{L2}} \times \epsilon_{\text{TPC}} \times \epsilon_R \times \epsilon_{dE/dx} \times \epsilon_{E/p}$, where the symbols are as follows. ϵ_{geo} is the BEMC geometrical acceptance. ϵ_{vertex} is the vertex-finding efficiency. ϵ_{L0} and ϵ_{L2} are the trigger efficiencies for L0 and L2, respectively. ϵ_{TPC} is the TPC geometrical acceptance times tracking efficiency for reconstructing both daughters in the TPC. ϵ_R is the TPC-BEMC η-φ matching efficiency. $\epsilon_{dE/dx}$ is the electron identification efficiency from the specific ionization requirement, and $\epsilon_{E/p}$ is the electron identification efficiency from the E/p selection.

We find for the cross section at midrapidity in $\sqrt{s} = 200$ GeV $p + p$ collisions the result

TABLE IV. Systematic uncertainties on the measurement of the Υ cross section.

Quantity	Value	Syst. uncertainty on $d\sigma/dy$ (%)
$N_{+-} - 2\sqrt{N_{++}N_{--}}$	82.7	$^{+0}_{-9}$
$\mathcal{L}$	7.9 pb^{-1}	± 7
ϵ_{BBC}	0.87	± 9
ϵ_{geo}	0.57	$^{+3.0}_{-1.7}$
ϵ_{vertex}	0.96	± 1.0
ϵ_{L0}	0.43	$^{+7.5}_{-5.9}$
ϵ_{L2}	0.85	$^{+0.7}_{-0.2}$
ϵ_{TPC}	0.85^2	$2 \times \pm 5.8$
ϵ_R	0.93^2	$2 \times^{+1.1}_{-0.2}$
$\epsilon_{dE/dx}$	0.84^2	$2 \times \pm 2.4$
$\epsilon_{E/p}$	0.93^2	$2 \times \pm 3.0$
Combined		$^{+22.8}_{-24.1}$ pb

$$\sum_{n=1}^{3} \mathcal{B}(nS) \times \sigma(nS) = 114 \pm 38^{+23}_{-24} \text{ pb}. \qquad (8)$$

The uncertainties quoted are the 33% stat + fit uncertainty (mentioned in the discussion of Table III) and the systematic uncertainty, respectively.

The major contributions to the systematic uncertainty are as follows: the uncertainty in the choice of bin-counting method, the uncertainty in the integrated luminosity, the uncertainty in the BBC efficiency for $p + p$ NSD events and the uncertainty in the L0 trigger efficiency for Υ events. The polarization of the Υ states also affects the estimation of the geometrical acceptance. We estimate this uncertainty by comparing simulations of fully longitudinal and fully transverse decays and comparing the acceptance of these cases with the unpolarized case. A list of all corrections and systematic uncertainties in the procedure to extract the cross section is compiled in Table IV. The combined systematic uncertainty is obtained by adding all the sources in quadrature. Note that the single-particle efficiencies enter quadratically when reconstructing di-electron pairs, so we multiply the single-particle uncertainty by a factor of 2 when estimating the pairwise uncertainty.

The result we obtain for the cross section is shown in Fig. 13, where the datum point given by the star symbol is our measurement, and the error bars and the box depict the statistical and systematic uncertainties, respectively. To illustrate the acceptance in rapidity, we also show the unlike-sign pairs after like-sign background subtraction, $N_{+-} - 2\sqrt{N_{++}N_{--}}$, in the Υ region $8 < m_{ee} < 11$ GeV/c^2 as a hashed histogram. The scale on the right axis of the figure is used for the counts in the histogram, and the scale in the left axis of the figure is used for the cross section. We compare our measurement with NLO CEM predictions [32] of the Υ(1S) rapidity distribution.
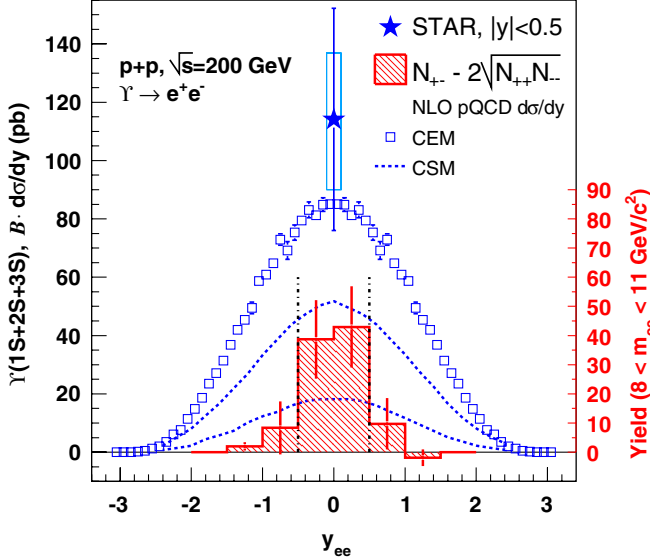
FIG. 13 (color online). The STAR measurement of the mid-rapidity $\Upsilon(1S + 2S + 3S)$ cross section times branching ratio into electrons (star). Error bars are statistical, the box shows the systematic uncertainty, and the scale is given by the left axis. The raw yield vs y is shown by the histogram at the bottom (diagonal-line fill pattern), with the scale on the right axis. The cross section was calculated from the yield between the vertical dot-dashed lines, $|y_{ee}| < 0.5$. The open squares are from an NLO CEM calculation, and the two dotted lines give the limits for the prediction from a NLO CSM calculation of the Υ cross section (see text).
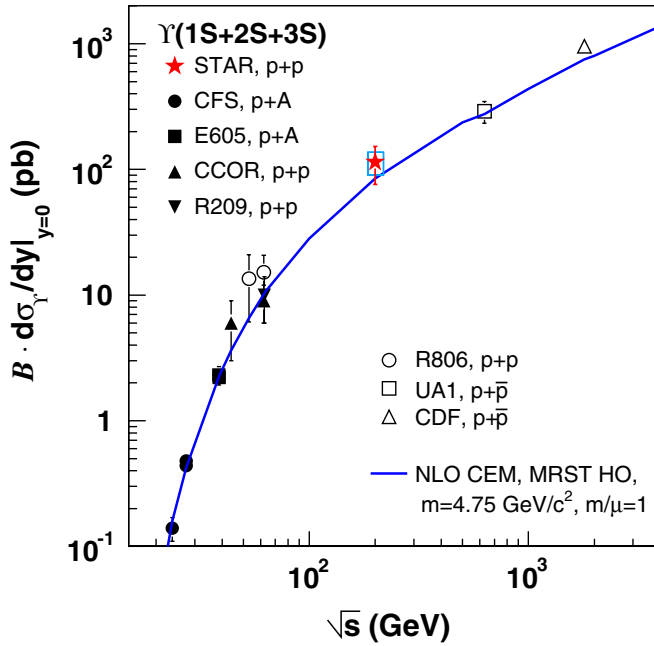

FIG. 14 (color online). Evolution of the $\Upsilon(1S + 2S + 3S)$ cross section with center-of-mass energy for the world data and an NLO CEM calculation. The error bars on the STAR datum point are statistical and systematic as in Fig. 13.

Since we measure all three states and only in the dielectron channel, the calculation of the $\Upsilon(1S)$ is scaled by a factor

$$\frac{\mathcal{B}(1S) \times \sigma(1S) + \mathcal{B}(2S) \times \sigma(2S) + \mathcal{B}(3S) \times \sigma(3S)}{\sigma(1S)}$$

(9)

in order to compare it to our measurement of the cross section for all three states. The branching ratios and cross sections used for these scale factors are those from Table II. The calculation is in agreement with our measurement. The two dotted lines in the plot are the upper and lower bounds of the cross section obtained from a calculation in the CSM for direct $\Upsilon(1S)$ production [18] based on NLO code developed for quarkonium production at hadron colliders [33]. Since the calculation is for the 1S state alone and for direct Υ production (ignoring feed-down from P states), to compare to our measurement, which includes all 3 states and feed-down contributions, the values from the calculation were divided by a factor 0.42 to account for this (see Ref. [18] for details). The bounds in the calculation are obtained by varying the bottom quark mass and the renormalization and factorization scales. The CSM prediction is lower than our data, indicating that additional contributions are needed beside production via color singlet.

In Fig. 14, we also compare our $\Upsilon(1S + 2S + 3S)$ result with measurements done in $p + A$, $p + p$, and $p + \bar{p}$ collisions at center-of-mass energies ranging from 20 GeV up to 1.8 TeV [24,29,34–41], and to NLO CEM predictions [16] for a wide range of center-of-mass energies.

Our result is consistent with the overall trend and provides a reference for bottomonium production at the top RHIC energy.

VII. CONCLUSIONS

The STAR experiment has measured the $\Upsilon(1S + 2S + 3S) \rightarrow e^+e^-$ cross section at midrapidity, $|y_{ee}| < 0.5$, in $p + p$ collisions at $\sqrt{s} = 200$ GeV to be $(\mathcal{B} \times d\sigma/dy)^{1S+2S+3S} = 114 \pm 38$ (stat + fit)$^{+23}_{-24}$ (syst) pb. Calculations done in the color evaporation model at NLO are in agreement with our measurement, while calculations in the color singlet model underestimate our cross section by $\approx 2\sigma$. Our result is consistent with the trend as a function of center-of-mass energy based on data from other experiments. We report a combined continuum cross section, Drell-Yan plus $b\text{-}\bar{b} \rightarrow e^+e^-$, measured in the kinematic range $|y_{ee}| < 0.5$ and $8 < m_{ee} < 11$ GeV/c^2, of $(\sigma_{DY} + \sigma_{b\text{-}\bar{b}}) = 38 \pm 24$ pb. The STAR measurement presented here will be used as a baseline for studying cold and hot nuclear matter effects in $d + Au$ and $Au + Au$ collisions, as the relatively clean environment provided by the STAR high-mass dielectron trigger permits the approach outlined in this paper to be deployed up to the most central $Au + Au$ collisions. With increased luminosity, a better determina-

tion of the cross section, its $p_\perp$ dependence, and a separation of the 2S and 3S states will be possible. The projected luminosity upgrades to RHIC should increase the ϒ yield to ≈ 8300 in $p + p$ and $\approx 11\,200$ in Au + Au collisions during one RHIC year [16]. The increased statistics will greatly reduce the uncertainty in the determination of the continuum cross section and will allow a thorough study of the bottomonium sector by resolving the 2S and 3S states.

ACKNOWLEDGMENTS

[1] T. Matsui and H. Satz, Phys. Lett. B **178**, 416 (1986).
[2] S. Gavin, M. Gyulassy, and A. Jackson, Phys. Lett. B **207**, 257 (1988).
[3] J.-P. Blaizot and J.-Y. Ollitrault, Phys. Rev. D **39**, 232 (1989).
[4] L. Grandchamp, R. Rapp, and G. E. Brown, Phys. Rev. Lett. **92**, 212301 (2004).
[5] R. L. Thews *et al.*, Eur. Phys. J. C **43**, 97 (2005).
[6] A. Andronic *et al.*, Nucl. Phys. **A789**, 334 (2007).
[7] S. Digal, P. Petreczky, and H. Satz, Phys. Rev. D **64**, 094015 (2001).
[8] J. F. Gunion and R. Vogt, Nucl. Phys. **B492**, 301 (1997).
[9] M. Cacciari, P. Nason, and R. Vogt, Phys. Rev. Lett. **95**, 122001 (2005).
[10] Z. w. Lin and C. M. Ko, Phys. Lett. B **503**, 104 (2001).
[11] D. M. Alde *et al.*, Phys. Rev. Lett. **66**, 2285 (1991).
[12] A. Mocsy and P. Petreczky, Phys. Rev. Lett. **99**, 211602 (2007).
[13] S. Digal, P. Petreczky, and H. Satz, Phys. Lett. B **514**, 57 (2001).
[14] C.-Y. Wong, Phys. Rev. C **72**, 034906 (2005).
[15] A. Mocsy and P. Petreczky, Phys. Rev. D **77**, 014501 (2008).
[16] A. D. Frawley, T. Ullrich, and R. Vogt, Phys. Rep. **462**, 125 (2008).
[17] T. Kollegger, Ph.D. thesis, Johann Wolfgang Goethe-Universität Frankfurt am Main, 2005.
[18] S. J. Brodsky and J. P. Lansberg, Phys. Rev. D **81**, 051502 (2010).
[19] M. Anderson *et al.*, Nucl. Instrum. Methods Phys. Res., Sect. A **499**, 659 (2003).
[20] M. Beddo *et al.*, Nucl. Instrum. Methods Phys. Res., Sect. A **499**, 725 (2003).
[21] J. Kyriluk (STAR Collaboration), in *Proceedings of the 16th International Spin Physics Symposium* (World Scientific, Singapore, 2005), p. 718.
[22] J. Adams *et al.* (STAR Collaboration), Phys. Rev. Lett. **91**, 172302 (2003).
[23] F. S. Bieser *et al.*, Nucl. Instrum. Methods Phys. Res., Sect. A **499**, 766 (2003).
[24] D. E. Acosta *et al.* (CDF Collaboration), Phys. Rev. Lett. **88**, 161802 (2002).
[25] T. Sjostrand, arXiv:0809.0303.
[26] R. Field and R. C. Group (CDF Collaboration), arXiv:hep-ph/0510198.
[27] C. Amsler *et al.* (Particle Data Group), Phys. Lett. B **667**, 1 (2008).
[28] A. D. Martin, R. G. Roberts, W. J. Stirling, and R. S. Thorne, Eur. Phys. J. C **4**, 463 (1998).
[29] G. Moreno *et al.*, Phys. Rev. D **43**, 2815 (1991).
[30] M. C. Abreu *et al.* (NA38 and NA50 Collaborations), Eur. Phys. J. C **14**, 443 (2000).
[31] J. Gaiser, Ph.D. thesis, Stanford University [Report No. SLAC-R-255, Appendix F, p. 178].
[32] R. Vogt, Calculations vs $\sqrt{s}$ in [16], calculations vs rapidity and for Drell-Yan shown in RHIC-II Science Workshop, 2005 [http://rhicii-science.bnl.gov/heavy/doc/April05Meeting/].
[33] J. M. Campbell, F. Maltoni, and F. Tramontano, Phys. Rev. Lett. **98**, 252002 (2007).
[34] J. K. Yoh *et al.*, Phys. Rev. Lett. **41**, 684 (1978); **41**, 1083 (E) (1978).
[35] K. Ueno *et al.*, Phys. Rev. Lett. **42**, 486 (1979).
[36] S. Childress *et al.*, Phys. Rev. Lett. **55**, 1962 (1985).
[37] T. Yoshida *et al.*, Phys. Rev. D **39**, 3516 (1989).
[38] L. Camilleri, in *Proceedings of the 9th International Symposium on Lepton and Photon Interactions at High Energy, Batavia, Illinois, 1979* (Fermilab, 1979), p. 228.
[39] C. Kourkoumelis *et al.*, Phys. Lett. **91B**, 481 (1980).
[40] A. L. S. Angelis *et al.* (CCOR Collaboration), Phys. Lett. **87B**, 398 (1979).
[41] C. Albajar *et al.* (UA1 Collaboration), Phys. Lett. B **186**, 237 (1987).